THE JOURNAL OF PHYSICAL CHEMISTRY C
A JOURNAL OF THE AMERICAN CHEMICAL SOCIETY

pubs.acs.org/JPCC

Article

Quantitative Local Conductivity Imaging of Semiconductors Using Near-Field Optical Microscopy

Published as part of The Journal of Physical Chemistry virtual special issue "Nanophotonics for Chemical Imaging and Spectroscopy".

Earl T. Ritchie,[†] Clayton B. Casper,[†] Taehyun A. Lee, and Joanna M. Atkin*

Cite This: *J. Phys. Chem. C* 2022, 126, 4515–4521

Read Online

ACCESS | Metrics & More | Article Recommendations | Supporting Information

ABSTRACT: We demonstrate contactless, nanoscale measurements of local conductivity, free carrier density, and mobility using phase-resolved infrared (IR) scattering-type near-field optical microscopy (s-SNOM). Our approach extracts quantitative conductivity information by combining analytical and finite-element methods to predict the scattered near-field amplitude and phase for specific sample geometries, without relying on bulk mobility assumptions or empirical fitting parameters. We find that the finite-dipole model (FDM) overestimates the expected near-field amplitude and phase in nonplanar or nanostructured materials, so we employ finite-element modeling to choose appropriate corrections to the FDM and account for sample geometry. The model is validated using a silicon calibration sample, and our results return the free carrier concentration expected based on the encoded dopant profile. Mobility and conductivity are also found to be in good agreement with established models for bulk silicon. This work demonstrates the potential of IR s-SNOM to perform quantitative local conductivity measurements, including the separation of free carrier density and electronic mobility, and represents a step toward the goal of quantitative carrier profiling and mobility mapping using s-SNOM.

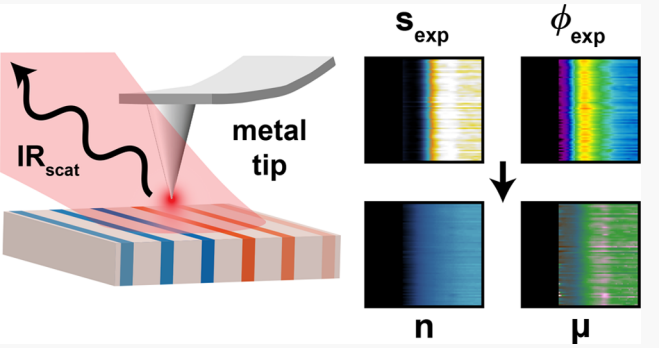

INTRODUCTION

Semiconducting materials are critical building blocks of modern technology, forming the basis for a wide array of electronics and communications devices. The functionality of these devices relies on the precise modification of the local electrical conductivity, which can be finely tuned in semiconductors with impurity atoms (dopants), temperature, and photoexcitation.[1] As such, the ability to quantitatively measure the nanoscale conductivity (σ) and the mobility (μ) of a material is important for the design and manufacture of precisely controlled devices, in particular for novel materials, synthesis, and architectures. While the electronic mobility is critical for performance metrics such as switching speeds and the frequency response of devices, characterizing mobility variations remains extremely challenging.

Scattering-type scanning near-field optical microscopy (s-SNOM) is a recently developed scanning probe technique that has been successfully used to study semiconducting nanomaterials.[2−9] Similar to other scanning probe techniques such as conductive atomic force microscopy (c-AFM), s-SNOM has the advantage of being nondestructive, and it provides a means to directly probe the local free carrier concentration with high spatial resolution.[10−12] Conductivity imaging using s-SNOM is based on free carrier absorption in the infrared (IR) and terahertz (THz) spectral regions[13,14] and has been utilized previously for visualizing material contrast in complex nanostructures, such as the dielectric and semiconducting regions of nanotransistors[3,15] and nanowire superlattices.[5,8,10−12,16] However, previous s-SNOM studies on semiconducting nanostructures were largely qualitative in nature, involving simplifying assumptions such as bulk mobility, without calibration or comparison to complementary techniques. Furthermore, many previous s-SNOM experiments have not accounted for geometric effects, which often dominate the properties of nanostructured materials.[17−19] Thus, there is clear potential to improve the accuracy and validation of s-SNOM measurements of semiconductors and especially low-dimensional materials.

Received: December 12, 2021
Revised: February 7, 2022
Published: February 25, 2022

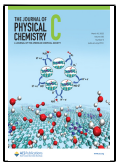

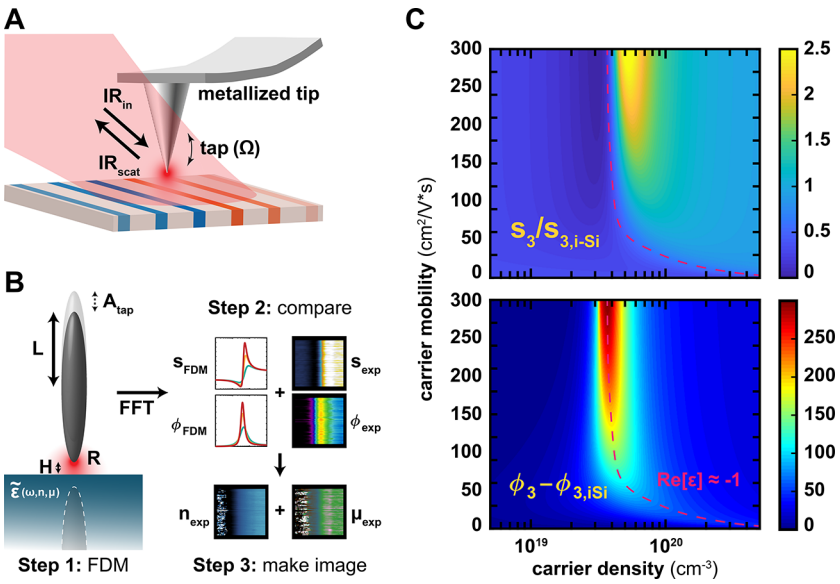

Figure 1. s-SNOM for optical conductivity measurements. (A) Schematic of IR s-SNOM. (B) Illustration of the method used for extracting carrier density and mobility from near-field images, based on finite-dipole model (FDM) parameters discussed in the text. (C) Dependence of near-field amplitude (top) and phase (bottom) on carrier density and mobility for n-Si. The magenta dashed line indicates the location of the tip−sample resonance for bulk Si. Values were calculated using the FDM with ω = 940 cm^{-1}, t_{SiO_2} = 3 nm, A_{tap} = 25 nm, $n\Omega$ = 3, and $g = 0.98\epsilon^{0.14i}$. Plots are normalized to intrinsic Si (no doping).

Here we demonstrate that phase-resolved IR s-SNOM measurements can be used to determine the complete local conductivity response, separating the free carrier and mobility contributions in semiconductors. We validate our method with measurements on a known calibration standard[20,21] and find good agreement with the previous empirical conductivity models. The experiments in this paper represent a significant step forward in using IR s-SNOM as a method for quantitative mapping of the conductivity in both n-type and p-type semiconductors with spatially varying encoded doping. Furthermore, our measurements demonstrate s-SNOM's capability to perform nanoresolved measurements of variations in a material's mobility, enabling direct correlation of morphological properties with charge transport.

METHODS

Near-Field Determination of Conductivity. Figure 1A illustrates a typical IR s-SNOM experiment in which a metallized AFM tip acts as a nanoantenna to focus and scatter incident IR light. This scattered light is collected simultaneously with AFM topography, homodyned with a reference signal to deduce the complex near-field optical response, and demodulated at higher harmonics of the tip tapping amplitude to extract the near-field signal. We perform our experiments at a single IR frequency, 940 cm^{-1}. Other details of the experiment are discussed in the Supporting Information.

The s-SNOM measurement produces two high-resolution (∼10−20 nm) near-field images, conventionally near-field amplitude and phase, which are related to the complex permittivity of the surface. However, extracting material properties, specifically the free carrier concentration n and carrier mobility μ in a semiconductor, from these near-field images requires a model to describe the convolutional tip−sample interaction. Here, we use the finite-dipole model (FDM),[22] due to its accuracy and fast computation time.[10,23,24] Additionally, we employ a multilayer (ML) extension to the FDM in order to account for a layer of native oxide on the silicon surface.[25] In the FDM, the tip is approximated as a perfectly conducting ellipsoid with semiaxis length L and apex radius R placed a distance H away from the sample surface (Figure 1B). The FDM treats the field interactions between the ellipsoid and sample with the method of image charges and introduces a parameter g, the ratio of near-field induced charge to total charge within the ellipsoid, to model the exponential decay of the near-field interaction. The sample dielectric properties are introduced to the tip−sample modeling through the parameter β, which is directly related to the complex permittivity ϵ. We describe the IR permittivity of silicon using the Drude model of conductivity,[26,27] which can be expressed in terms of free carrier concentration n and carrier mobility μ.

Most often the FDM parameters are determined through fitting to experimental near-field distance-dependent curves or spectra,[22] which has resulted in a range of FDM parameter values reported in the literature that prevent quantitative analysis. Here, we deduce values for parameters without reference to the near-field results, in order to generalize our model for systems where the conductivity response may be unknown. For our modeling, we use a tip apex radius of R = 25 nm, based on the measured AFM topography. Because the tapping amplitude has a pronounced effect on the scale of the near-field amplitude and phase (see supplement), we derive a tapping amplitude (A_{tap}) for each scan from AFM approach curves.[28] Two parameters, however, cannot be chosen based on independent experimental analysis: the ellipsoid semiaxis length L and the near-field induced charge g. These are the two most sensitive parameters in the model, as demonstrated in Figure S1 and the discussion in the Supporting Information. For example, we see a 2-fold increase in the near-field amplitude and a 50° phase increase as g increases from 0.6 to 0.9. Varying L from 150 to 600 nm causes a 30° phase increase and a 1.5 increase in amplitude at their respective maxima. The choice of these two parameters is therefore critical to accurately extracting information, such as the conductivity, from near-field results on semiconducting systems.

https://doi.org/10.1021/acs.jpcc.1c10498
J. Phys. Chem. C 2022, 126, 4515−4521

To find reasonable values for g and L in the FDM, we employ finite-element methods, which allow us to accurately model the near-field optical response between the tip and sample for specific conditions. These results can then be compared to the results obtained in the analytical FDM under the same conditions, and parameters were chosen to best fit the computational results. For consistency with the FDM calculations, we model the tip in COMSOL as a conductive spheroid (R = 25 nm) modulating above the surface with a tapping amplitude A_{tap} and $n\Omega$ = 3 demodulation order (see Supporting Information for simulation details). To replicate the large near-field amplitudes extracted from the finite element analysis, we choose L = 600 nm as the best value in the FDM. Larger values for L are incompatible with the requirement that $L \ll \lambda$.[23,29] With these parameters, we find an optimal value of $g = 0.98e^{0.14i}$ for a doped Si substrate with a dopant concentration in the range of 1×10^{18} cm^{-3} to 1×10^{21} cm^{-3}.

On the basis of this rationalization of parameters, we can use the FDM to accurately calculate near-field amplitude and phase for comparison with experimental results, and rapid conversion of near-field images to material properties. Figure 1C shows the predicted third harmonic near-field amplitude (s_3) and phase (ϕ_3) signals for planar, doped silicon under mid-IR (940 cm^{-1}) illumination, based on the ML-FDM as a function of both carrier density and mobility. The parameters chosen for this modeling are as derived above: R = 25 nm, L = 600 nm, t_{SiO_2} = 3 nm, A_{tap} = 25 nm, and $g = 0.98e^{0.14i}$. The results are normalized to the response for intrinsic silicon (ε = 11.68). In bulk silicon, the mobility decreases with increasing doping, due to the increased scattering from ionized dopant atoms.[30] For our analysis, we make no *a priori* assumptions about the mobility and instead allow carrier density and mobility to vary independently. For a given mobility, the near-field amplitude for dopant concentrations above 1×10^{19} cm^{-3} approximates a dispersive line shape. The near-field phase ϕ_3 approximates a Lorentzian line shape. This behavior corresponds to the tip−sample resonance at Re[ε] = −1, denoted by the magenta line on the graph. As the mobility decreases, the magnitude of the peak decreases and the line width increases, and the resonance condition shifts to higher carrier densities. The maximum near-field phase and amplitude increase as the mobility increases, though it should be noted that the range of mobilities calculated for the model extends beyond that expected for bulk mobility in this doping range.[30]

Within the sensitivity range of degenerate doping, 1×10^{19} cm^{-3} to 1×10^{20} cm^{-3}, there exist a unique near-field amplitude and phase for every value of n and μ, which allows collected near-field channels to be directly converted to n and μ using our model for the tip−sample interaction. In order to perform local conductivity mapping, we determine a best-fit n and μ for a given experimental near-field amplitude and phase pair by minimizing the percent difference with the FDM results. Pixel-by-pixel iteration of this method generates maps of n and μ, which can be further used to calculate a conductivity map $\sigma = ne\mu$ (Figure 1B). For cases outside our sensitivity range (nondegenerate or very high degenerate doping), the minimized percent error is large because there is no longer a unique n and μ for a given amplitude and phase.

RESULTS

We validate our modeling approach by testing a commercially available doping calibration standard (Infineon Technologies),[20,21] which allows us to compare our results to previous resistivity measurements (Figure 2). The calibration standard consists of a lightly p-doped wafer (1×10^{15} dopants/cm^3, with a series of implanted phosphorus and boron stripes with a constant pitch. The implantation is relatively homogeneous over the first 200 nm depth.[20]

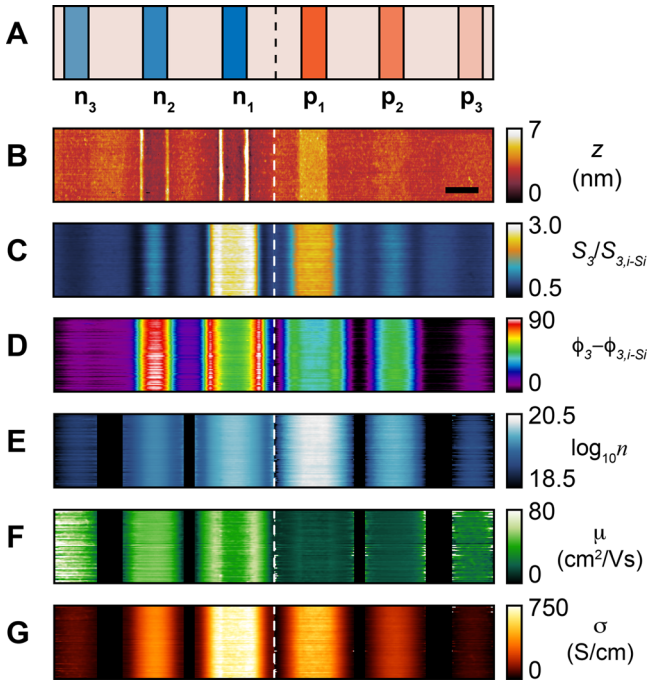

Figure 2. Method validation using a Si calibration wafer (Infineon). (A) Dopant scheme, (B) measured topography (nm, scale bar = 1 μm), (C) near-field amplitude, and (D) near-field phase (deg) normalized to intrinsic Si. The dotted white line demarcates the transition from n-type doping to p-type. (E) Carrier density (cm^{-3}, log scale), (F) carrier mobility (cm^2/(V·s)), and (G) the total conductivity of the wafer (S/cm) were extracted from the near-field images using the method outlined in the text.

s-SNOM measurements on the calibration sample were conducted at 940 cm^{-1} and normalized to the lightly doped silicon regions. The near-field response is constant for doping concentrations below ~1×10^{17} for our probe wavelength, and therefore these lightly doped silicon regions are equivalent to the intrinsic silicon normalization used in the modeling. Parts B, C, and D of Figure 2 respectively show the topography, near-field amplitude, and near-field phase of a representative scan at 940 cm^{-1}. The three highest concentration sections for both n-type and p-type doping are within the sensitivity range of our measurements (Figure 2A; n_1 and p_1, 1×10^{20} cm^{-3}; n_2 and p_2, 4×10^{19} cm^{-3}; and n_3 and p_3, 1×10^{19} cm^{-3}). All six high doping regions can be distinguished in both near-field amplitude and phase, with n_1 and p_1 showing the strongest contrast and with very weak contrast for the lowest-doped n_3 and p_3 sections. We note that the highly doped sections appear wider in the near-field response than the schematic and topography, similar to previous scanning probe measurements.[21] This effect can be attributed to dopant diffusion during a dopant activation step when the wafer was prepared.

https://doi.org/10.1021/acs.jpcc.1c10498
J. Phys. Chem. C 2022, 126, 4515−4521

This explanation is consistent with the observed broader stripes for highly doped regions, where more diffusion into adjacent low-doped regions would be expected. While the central portion of each dopant region appears to have a relatively homogeneous near-field response, the edges of regions show variations, in particular for the highest doped areas.

Parts E, F, and G of Figure 2 respectively show the n, μ, and σ maps generated by our postprocessing method. The lightly doped regions between each implanted section, which are outside our sensitivity range, have been blanked for clarity. We observe that the extracted free carrier concentration, n, is highest for regions n_1 and p_1 and lower for the other regions, as expected. All values for free carrier concentration fall within the range 10^{18} to 2×10^{20} dopants/cm^3. The mobility appears to be highest for the lower doped regions p_3 and n_3 and is relatively consistent for each region except in the case of the n_1 region. For this highly doped region, the decrease in doping concentration n at the edges of the stripe is correlated with an increase in mobility, consistent with the diffusion effect. Region n_1 shows the highest conductivity, and both the p- and n-type regions show the expected decreasing conductivity with decreasing free carrier concentration.

We analyze the conductivity maps to extract quantitative information for each region and compare our results to bulk resistivity models. Parts A and B of Figure 3 show the extracted carrier density and mobility for the calibration sample for the n-type and p-type regions, respectively. Each data point represents a pixel in a 15 by 80 rectangle in the specified doping section. Comparison to the encoded doping concentrations (vertical dashed lines) demonstrates that our method correctly extracts the expected carrier density for each doping section.[20,21] The range of doping concentrations observed for each region is relatively small, while the variation in mobility is much larger. This observation may relate to the diffusion effects discussed above. Furthermore, these extracted mobility values are reduced by approximately 20−40% in comparison to models for bulk silicon.[30]

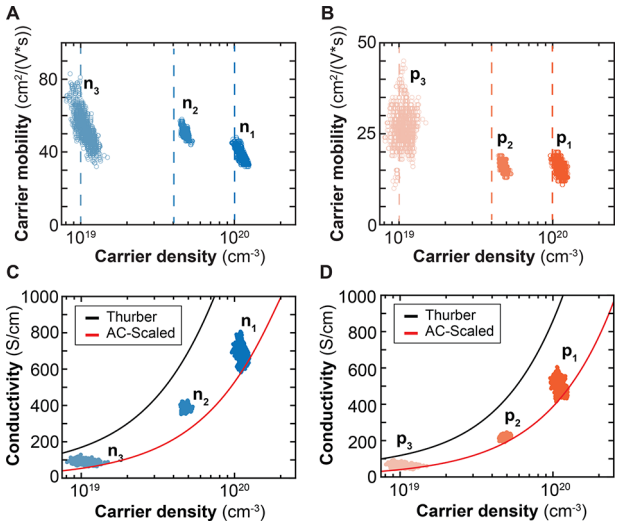

Figure 3. Calculated carrier density and mobility for doped silicon calibration sample, extracted from images in Figure 2. Scatter plot of mobility vs carrier density for each pixel in a 15 × 80 rectangle for each n-type (A) and p-type (B) doping section. The extracted values of free carrier concentration (circles) agree very well with the calibrated doping concentrations (vertical dashed lines). The mobility varies significantly across the regions and is lower than expected for bulk DC mobility. (C, D) Extracted conductivity for the same regions as in panels A and B, showing the increasing conductivity with increasing free carrier density. The results are compared to the Thurber conductivity model for silicon[31,32] without (black) and with (red) an AC correction. Good agreement is seen with the expected conductivity once the AC correction factor is applied.

In order to explain this observation, we consider the near-field derived conductivity values (Figure 3C,D) and predicted conductivity for bulk silicon for both the n- and p-type doping (black line).[31,32] Our experimental results follow the expected trend of bulk silicon, but with reduced conductivity for all doping densities, arising from the lower mobilities. This effect is related to the spectral regime of our measurements, since the conductivity of silicon decreases from the DC value as the measurement frequency (ω) approaches the scattering time (τ) of free carriers. For an incident frequency of 940 cm^{-1} and the dopant densities considered in this work, $\omega\tau \approx 0.3$, indicating that an AC correction must indeed be applied.[27] The resulting AC conductivity, reflecting the reduced mobility, is shown as the red line in Figure 3C,D and demonstrates excellent agreement with our experimental results.

Having validated the FDM parameter set using a planar calibration sample, we can consider how our analysis must be modified for nanostructured systems such as nanowires, nanotubes, and heterostructures, which are being studied for the next generation of electrical, photovoltaic, and photonic devices. Since the FDM was formulated assuming a perfectly flat and infinitely deep sample, care must be taken when attempting to use the model to extract quantitative information from nanostructures. Employing the multilayer-FDM allows surface layers to be included, but this still assumes a flat sample, leading to overestimation of the degree of coupling between the tip and a thin and/or nonplanar sample. We therefore further employ COMSOL simulations to study how geometry impacts the near-field signal in a cylinder-on-a-plane system, as compared to a planar system (Figure 4) and use these results to add a correction to the FDM for measurements on nanowire devices. This approach maintains the efficient computation of the FDM while expanding its scope to more complex systems. For these simulations, we again model the tip as a conductive spheroid with the same geometry as the planar system (L = 600 nm, R = 25 nm) modulating above the surface with a tapping amplitude A_{tap} and $n\Omega$ = 3 demodulation order (Figure 4A). For the carrier concentration range 1×10^{17} cm^{-3} to 1×10^{21} cm^{-3}, we simulate four different sample geometries: doped-Si cylinders with diameters 50, 100, 150,

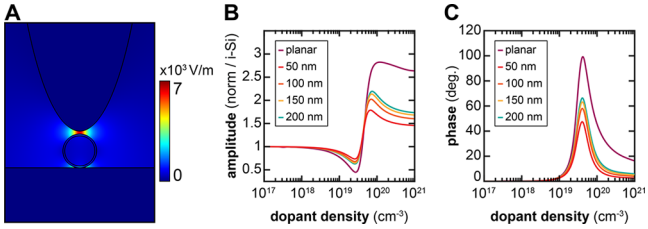

Figure 4. Determination of near-field induced charge (g) for planar and nonplanar geometries. (A) Simulated vertical component of the electric field (V/m) of a Pt ellipse over a doped SiNW with d = 50 nm and a 3 nm layer of oxide. Simulated demodulated (n = 3 Ω, A_{tap} = 35 nm) near-field amplitude (B) and phase (C) for various nanowire diameters. Results are normalized to the $N = 1 \times 10^{17}$ cm^{-3} case.

https://doi.org/10.1021/acs.jpcc.1c10498
J. Phys. Chem. C 2022, 126, 4515−4521

200 nm, with a 3 nm overlayer of SiO_2, on a gold substrate. Parts B and C of Figure 4 show the resultant demodulated near-field amplitude and phase from the COMSOL simulations. We find that the near-field amplitude and phase response in nanowire simulations decrease as the diameter decreases. Furthermore, we find that when the FDM is not modified to account for the sample geometry, the predicted amplitude and phase response are overestimated in our nanostructured samples when compared to planar Si. By decreasing the value for g in the FDM as the diameter decreases, we can match the results from COMSOL modeling and obtain a more realistic description of the near-field between the tip and a cylindrical silicon nanowire. We choose to modify g since we expect the distribution of near-field induced charges at the tip apex to be affected by the fact that there is less material directly underneath the tip when above a nanostructured sample. We can therefore use the nanowire diameter and A_{tap} as input parameters for our postprocessing algorithm, resulting in a change in near-field induced charge from $g = 0.75e^{0.18i}$ at 200 nm to $g = 0.5e^{0.23i}$ for 50 nm diameters at A_{tap} = 35 nm (more details in the Suppporting Information).

DISCUSSION

We note that our measurements and calculations were performed using only a single wavelength of 10.63 μm (940 cm^{-1}), simplifying both experimental and computational processes. However, this choice of wavelength limits the sensitivity range to degenerate doping concentrations in silicon of 10^{18}−10^{21} dopants/cm^3. To extract quantitative information for lower doping concentrations in silicon, longer wavelengths (lower frequencies) must be employed, and potentially for THz measurements, additional band-bending effects should be incorporated.[19]

For the mid-infrared spectral range, additional considerations on modeling can also apply. In particular, for semiconductors such as silicon the presence of an oxide layer can complicate the modeling. The Si−O phonon mode appears close to 1100−1200 cm^{-1} and affects the near-field response even for thin, native oxide layers.[12,33] While the ML-FDM allows for the incorporation of an oxide layer, as we have employed above, it applies only when the product of the reflection terms at the layer boundaries (air/oxide, and oxide/Si) is less than 1, i.e. $|\beta_{12}\cdot\beta_{23}| < 1$. As shown in Figure S2, this requirement is satisfied for all doping concentrations at our chosen frequency of 940 cm^{-1}. However, close to the Si−O resonance, the reflection terms rapidly exceed 1 even for a 3 nm oxide. This observation limits the applicability of the analytical ML-FDM for spectral ranges above ∼1000 cm^{-1} in silicon, hampering quantitative analysis. Similar issues will appear for other samples with phonon modes close to the excitation frequency, which can be the case for binary oxides and nitrides in the mid-IR. Quantitative analysis under these conditions will likely require more detailed FEM, increasing computational complexity and time scales for fitting.

We illustrated the potential for FEM-informed modeling of nanowire geometries, but our results are generally applicable to other nanostructured systems, including those with polaritonic or other non-Drude contributions to the signal. In particular, the ability to probe conductivity within a single nanostructure or on a subdomain level may be valuable for understanding the role of grain boundary scattering or finite size effects in conductivities extracted from bulk THz or infrared spectroscopy measurements. For finite size or polaritonic effects, however, we expect FEM to potentially reveal spatial variations that would then need to be incorporated into the FDM parameters in order to extract quantitive local permittivity information. Further work is needed to address this important problem.

Finally, our quantitative approach can also be applied to broadband measurements. The frequency response can provide additional information that could be valuable in establishing appropriate fitting parameters and exploring non-Drude contributions to the near-field response, without significantly reducing computational efficiency. Similar to single wavelength measurements, however, care must be taken in the vicinity of phonon modes.

CONCLUSIONS

In summary, we have developed a methodology for extracting quantitative conductivity maps from phase-resolved infrared near-field measurements. This was achieved by independently evaluating the local carrier density and mobility using a modified FDM and by validating our results against a well-known calibration standard. Our approach combines the advantages of two common modeling techniques: the speed and high-throughput of the analytical finite-dipole model with the accuracy and realistic geometry that come with electromagnetic finite-element modeling. We found that the FDM overestimates the near-field amplitude and phase in nanostructured systems and that we can use our finite-element model to improve accuracy and optimize FDM parameters for these scenarios. Furthermore, we are able to generate spatially resolved maps of the electronic mobility, previously inaccessible information that demonstrates the benefits of near-field microscopy. In this case, the use of silicon allows for comparison with well-controlled calibration standards and detailed knowledge of the relationship between mobility and conductivity at different doping concentrations, but this analysis can readily be extended to different semiconducting materials, including cases where the mobility-free carrier concentration is not established, as our analysis does not rely on *a priori* assumptions about mobility. This research represents a step toward the goal of fully quantitative s-SNOM for carrier profiling.

ASSOCIATED CONTENT

Supporting Information

The Supporting Information is available free of charge at https://pubs.acs.org/doi/10.1021/acs.jpcc.1c10498.

Additional information and figures related to analytical and numerical modeling, and full details of extracted carrier densities and mobilities (PDF)

AUTHOR INFORMATION

Corresponding Author

Joanna M. Atkin − *Department of Chemistry, University of North Carolina at Chapel Hill, Chapel Hill, North Carolina 27599, United States;* orcid.org/0000-0002-1211-5193; Email: jatkin@email.unc.edu

Authors

Earl T. Ritchie − *Department of Chemistry, University of North Carolina at Chapel Hill, Chapel Hill, North Carolina 27599, United States;* orcid.org/0000-0002-4113-756X

https://doi.org/10.1021/acs.jpcc.1c10498
J. Phys. Chem. C 2022, 126, 4515−4521

Clayton B. Casper − *Department of Chemistry, University of North Carolina at Chapel Hill, Chapel Hill, North Carolina 27599, United States;* orcid.org/0000-0001-9409-0155

Taehyun A. Lee − *Department of Chemistry, University of North Carolina at Chapel Hill, Chapel Hill, North Carolina 27599, United States*

Complete contact information is available at: https://pubs.acs.org/10.1021/acs.jpcc.1c10498

Author Contributions

†E.T.R. and C.B.C. contributed equally to this work.

Notes

The authors declare no competing financial interest.

■ ACKNOWLEDGMENTS

The work in this paper was supported by the National Science Foundation Chemical Measurement and Imaging program, under Grant CHE-1848278. The authors thank Dr. Samuel Berweger and NIST Boulder for the use of the Infineon calibration sample, and Dr. Taylor Teitsworth and Dr. James Cahoon for advice and comments.

■ REFERENCES

(1) Sze, S. M.; Ng, K. K. *Physics of Semiconductor Devices*, 3rd ed.; Wiley Limited, 2008; pp 1−68.

(2) Knoll, B.; Keilmann, F. Enhanced dielectric contrast in scattering-type scanning near-field optical microscopy. *Opt. Commun.* **2000**, *182*, 321−328.

(3) Huber, A. J.; Kazantsev, D.; Keilmann, F.; Wittborn, J.; Hillenbrand, R. Simultaneous IR Material Recognition and Conductivity Mapping by Nanoscale Near-Field Microscopy. *Adv. Mater.* **2007**, *19*, 2209−2212.

(4) Gigler, A. M.; Huber, A. J.; Bauer, M.; Ziegler, A.; Hillenbrand, R.; Stark, R. W. Nanoscale residual stress-field mapping around nanoindents in SiC by IR s-SNOM and confocal Raman microscopy. *Opt. Express* **2009**, *17*, 22351.

(5) Stiegler, J.; Tena-Zaera, R.; Idigoras, O.; Chuvilin, A.; Hillenbrand, R. Correlative infrared-electron nanoscopy reveals the local structure-conductivity relationship in zinc oxide nanowires. *Nat. Commun.* **2012**, *3*, 1131.

(6) Arcangeli, A.; Rossella, F.; Tomadin, A.; Xu, J.; Ercolani, D.; Sorba, L.; Beltram, F.; Tredicucci, A.; Polini, M.; Roddaro, S. Gate-Tunable Spatial Modulation of Localized Plasmon Resonances. *Nano Lett.* **2016**, *16*, 5688−5693.

(7) Choi, W.; Seabron, E.; Mohseni, P. K.; Kim, J. D.; Gokus, T.; Cernescu, A.; Pochet, P.; Johnson, H. T.; Wilson, W. L.; Li, X. Direct Electrical Probing of Periodic Modulation of Zinc-Dopant Distributions in Planar Gallium Arsenide Nanowires. *ACS Nano* **2017**, *11*, 1530−1539.

(8) Sakat, E.; Giliberti, V.; Bollani, M.; Notargiacomo, A.; Pea, M.; Finazzi, M.; Pellegrini, G.; Hugonin, J. P.; Weber-Bargioni, A.; Melli, M.; et al. Near-Field Imaging of Free Carriers in ZnO Nanowires with a Scanning Probe Tip Made of Heavily Doped Germanium. *Physical Review Applied* **2017**, *8*, 054042.

(9) Zhou, Y.; Chen, R.; Wang, J.; Huang, Y.; Li, M.; Xing, Y.; Duan, J.; Chen, J.; Farrell, J. D.; Xu, H. Q.; et al. Tunable Low Loss 1D Surface Plasmons in InAs Nanowires. *Adv. Mater.* **2018**, *30*, 1802551.

(10) Stiegler, J. M.; Huber, A. J.; Diedenhofen, S. L.; Gómez Rivas, J.; Algra, R. E.; Bakkers, E. P. A. M.; Hillenbrand, R. Nanoscale Free-Carrier Profiling of Individual Semiconductor Nanowires by Infrared Near-Field Nanoscopy. *Nano Lett.* **2010**, *10*, 1387−1392.

(11) Ritchie, E. T.; Hill, D. J.; Mastin, T. M.; Deguzman, P. C.; Cahoon, J. F.; Atkin, J. M. Mapping Free-Carriers in Multijunction Silicon Nanowires Using Infrared Near-Field Optical Microscopy. *Nano Lett.* **2017**, *17*, 6591−6597.

(12) Jung, L.; Pries, J.; Maß, T. W.; Lewin, M.; Boyuk, D. S.; Mohabir, A. T.; Filler, M. A.; Wuttig, M.; Taubner, T. Quantification of Carrier Density Gradients along Axially Doped Silicon Nanowires Using Infrared Nanoscopy. *ACS Photonics* **2019**, *6*, 1744−1754.

(13) Lahrech, A.; Bachelot, R.; Gleyzes, P.; Boccara, A. C. Infrared near-field imaging of implanted semiconductors: Evidence of a pure dielectric contrast. *Appl. Phys. Lett.* **1997**, *71*, 575−577.

(14) Buersgens, F.; Kersting, R.; Chen, H.-T. Terahertz microscopy of charge carriers in semiconductors. *Appl. Phys. Lett.* **2006**, *88*, 112115.

(15) Huber, a. J.; Wittborn, J.; Hillenbrand, R. Infrared spectroscopic near-field mapping of single nanotransistors. *Nanotechnology* **2010**, *21*, 235702.

(16) Lewin, M.; Baeumer, C.; Gunkel, F.; Schwedt, A.; Gaussmann, F.; Wueppen, J.; Meuffels, P.; Jungbluth, B.; Mayer, J.; Dittmann, R.; et al. Nanospectroscopy of Infrared Phonon Resonance Enables Local Quantification of Electronic Properties in Doped SrTiO 3 Ceramics. *Adv. Funct. Mater.* **2018**, *28*, 1802834.

(17) Björk, M. T.; Schmid, H.; Knoch, J.; Riel, H.; Riess, W. Donor deactivation in silicon nanostructures. *Nat. Nanotechnol.* **2009**, *4*, 103−107.

(18) Abate, Y.; Seidlitz, D.; Fali, A.; Gamage, S.; Babicheva, V.; Yakovlev, V. S.; Stockman, M. I.; Collazo, R.; Alden, D.; Dietz, N. Nanoscopy of Phase Separation in In x Ga 1- x N Alloys. *ACS Appl. Mater. Interfaces* **2016**, *8*, 23160−23166.

(19) Casper, C. B.; Ritchie, E. T.; Teitsworth, T. S.; Kabos, P.; Cahoon, J. F.; Berweger, S.; Atkin, J. M. Electrostatic tip effects in scanning probe microscopy of nanostructures. *Nanotechnology* **2021**, *32*, 195710.

(20) Schweinböck, T.; Hommel, S. Quantitative Scanning Microwave Microscopy: A calibration flow. *Microelectronics Reliability* **2014**, *54*, 2070−2074.

(21) Brinciotti, E.; Gramse, G.; Hommel, S.; Schweinboeck, T.; Altes, A.; Fenner, M. A.; Smoliner, J.; Kasper, M.; Badino, G.; Tuca, S.-S.; et al. Probing resistivity and doping concentration of semiconductors at the nanoscale using scanning microwave microscopy. *Nanoscale* **2015**, *7*, 14715−14722.

(22) Cvitkovic, A.; Ocelic, N.; Hillenbrand, R. Analytical model for quantitative prediction of material contrasts in scattering-type near-field optical microscopy. *Opt. Express* **2007**, *15*, 8550.

(23) Govyadinov, A. A.; Amenabar, I.; Huth, F.; Carney, P. S.; Hillenbrand, R. Quantitative Measurement of Local Infrared Absorption and Dielectric Function with Tip-Enhanced Near-Field Microscopy. *J. Phys. Chem. Lett.* **2013**, *4*, 1526−1531.

(24) Pollard, B.; Maia, F. C. B.; Raschke, M. B.; Freitas, R. O. Infrared Vibrational Nanospectroscopy by Self-Referenced Interferometry. *Nano Lett.* **2016**, *16*, 55−61.

(25) Hauer, B.; Engelhardt, A. P.; Taubner, T. Quasi-analytical model for scattering infrared near-field microscopy on layered systems. *Opt. Express* **2012**, *20*, 13173.

(26) Van Exter, M.; Grischkowsky, D. Carrier dynamics of electrons and holes in moderately doped silicon. *Phys. Rev. B* **1990**, *41*, 12140−12149.

(27) Levi, A. F. J. *Essential Classical Mechanics for Device Physics*; IOP Publishing, 2016; Chapter 6, pp 1−21.

(28) Wang, L.; Xu, X. G. Scattering-type scanning near-field optical microscopy with reconstruction of vertical interaction. *Nat. Commun.* **2015**, *6*, 8973.

(29) Fali, A.; Gamage, S.; Howard, M.; Folland, T. G.; Mahadik, N. A.; Tiwald, T.; Bolotin, K.; Caldwell, J. D.; Abate, Y. Nanoscale Spectroscopy of Dielectric Properties of Mica. *ACS Photonics* **2021**, *8*, 175−181.

(30) Masetti, G.; Severi, M.; Solmi, S. Modeling of carrier mobility against carrier concentration in arsenic-, phosphorus-, and boron-doped silicon. *IEEE Trans. Electron Devices* **1983**, *30*, 764−769.

(31) Thurber, W. R.; Mattis, R. L.; Liu, Y. M.; Filliben, J. J. Resistivity-Dopant Density Relationship for Boron-Doped Silicon. *J. Electrochem. Soc.* **1980**, *127*, 2291−2294.

(32) Thurber, W. R.; Mattis, R. L.; Liu, Y. M.; Filliben, J. J. Resistivity-Dopant Density Relationship for Phosphorus-Doped Silicon. *J. Electrochem. Soc.* **1980**, *127*, 1807−1812.
(33) Kischkat, J.; Peters, S.; Gruska, B.; Semtsiv, M.; Chashnikova, M.; Klinkmüller, M.; Fedosenko, O.; Machulik, S.; Aleksandrova, A.; Monastyrskyi, G.; et al. Mid-infrared optical properties of thin films of aluminum oxide, titanium dioxide, silicon dioxide, aluminum nitride, and silicon nitride. *Appl. Opt.* **2012**, *51*, 6789.

https://doi.org/10.1021/acs.jpcc.1c10498
J. Phys. Chem. C 2022, 126, 4515−4521